JACS Au
AN OPEN ACCESS JOURNAL OF THE AMERICAN CHEMICAL SOCIETY

pubs.acs.org/jacsau

Article

Dispersive 2D Triptycene-Based Crystalline Polymers: Influence of Regioisomerism on Crystallinity and Morphology

Siquan Zhang, Nie Fang, Xiaonan Ji, Yuefei Gu, Zhenchuang Xu, Shangbin Jin,* and Yanchuan Zhao*

Cite This: *JACS Au* 2022, 2, 1638−1650

Read Online

ACCESS | Metrics & More | Article Recommendations | Supporting Information

ABSTRACT: The merging of good crystallinity and high dispersibility into two-dimensional (2D) layered crystalline polymers (CPs) still represents a challenge because a high crystallinity is often accompanied by intimate interlayer interactions that are detrimental to the material processibility. We herein report a strategy to address this dilemma using rationally designed three-dimensional (3D) monomers and regioisomerism-based morphology control. The as-synthesized CPs possess layered 2D structures, where the assembly of layers is stabilized by relatively weak van der Waals interactions between C−H bonds other than the usual $\pi-\pi$ stackings. The morphology and dispersibility of the CPs are finely tuned via regioisomerism. These findings shed light on how to modulate the crystallinity, morphology, and ultimate function of crystalline polymers using the spatial arrangements of linking groups.

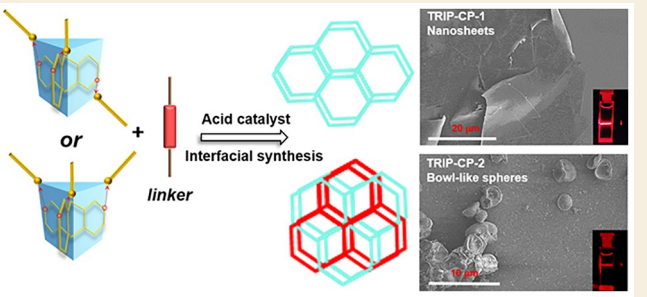

KEYWORDS: *dispersibility, triptycene, two dimensional, crystalline polymers, morphology, regioisomer*

INTRODUCTION

Crystalline polymers (CPs) assembled with covalent bonds often possess tunable chemical structures and large surface areas.[1−7] Among various CPs, covalent organic frameworks (COFs) have attracted increasing attention owing to their tailorable pore sizes and the ease of structural elaboration for applications ranging from gas adsorption, separation, catalysis, and optoelectronics to energy storage. To ensure a high crystallinity, COFs are usually constructed with planar building blocks of high symmetry.[8−17] As the $\pi-\pi$ stacking between the transient oligomeric intermediates is beneficial to self-correction and the formation of highly ordered assembly, highly crystalline layered two-dimensional (2D) COFs built solely with planar monomers are usually considered more accessible than those composed of three-dimensional (3D) structural units.[18−20] However, the strong $\pi-\pi$ stacking interactions between layers often lead to severe aggregation and poor dispersibility, which are detrimental to processibility and efficient substrate/molecule translocation within the material. As a consequence, there has been a growing interest in new strategies for accessing exfoliated COF nanosheets with a few layers ($n < 10$).[21−27] The treatment of COFs with strong acids, bases, or high-energy ultrasound is a viable way to destroy the interlayer interactions, affording dispersed COF nanosheets in solution. However, these methods are destructive and often lead to COFs of reduced structural integrity and crystallinity.[28,29] The molecular engineering of building blocks is another appealing strategy to modulate the interaction between layers, where the charge, steric hindrance, and dipole moments of the incorporated side chains influence the tendency of COFs to aggregate. This robust approach also offers opportunities to introduce in-pore functionalities that are essential for superior gas separation and catalysis. More recently, Loh et al demonstrated that the self-exfoliation of COFs can be achieved via the formation of backbone pseudorotaxanes, which allows the controllable partition of the interlayer space.[30]

In contrast to the intimate interlayer packings observed in many 2D COFs constructed with planar monomers, the use of 3D rigid building blocks with linking groups organized in proper arrangements may lead to a larger distance (>5 Å) between 2D interlayers, where the assembly of nanosheets is mainly stabilized by interactions between C−H bonds other than the usual $\pi-\pi$ stackings. This interesting packing pattern potentially leads to weakened interlayer interactions and thereby facilitates the exfoliation of COFs into thin nanosheets. As a consequence, COFs with such structural features may simultaneously possess high crystallinity and dispersibility.[31] When the ordered packings only exist for a few layers of the 2D polymer, the global crystallinity of the material decreases. In this case, these few-layered 2D nanosheets may be better

Received: April 5, 2022
Revised: May 10, 2022
Accepted: May 16, 2022
Published: June 23, 2022

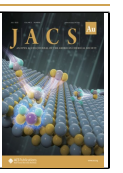

https://doi.org/10.1021/jacsau.2c00214
JACS Au 2022, 2, 1638−1650

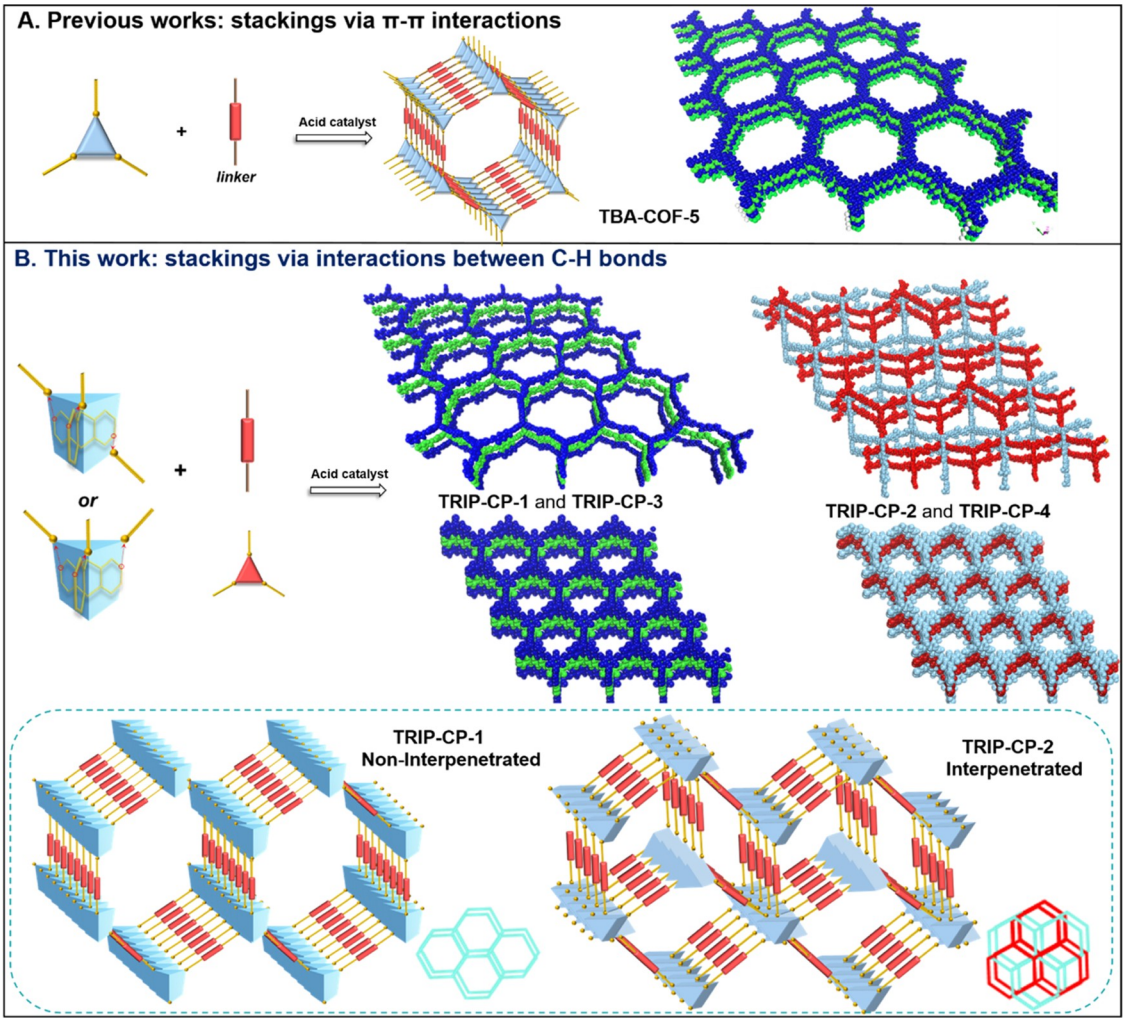

Figure 1. Comparisons between crystalline covalent organic polymers. (A) Crystalline 2D polymers assembled via $\pi-\pi$ stacking. (B) Regioisomeric triptycene-based crystalline polymer **TRIP-CP-1**, **TRIP-CP-2**, **TRIP-CP-3**, and **TRIP-CP-4** assembled via interactions between interlayered C−H bonds.

termed as 2D crystalline polymers (CPs) instead of 2D COFs.[32]

The triptycene-based monomers are ideal candidates to prepare the above-mentioned 2D COFs/CPs with C−H bonds facing the (100) planes. Owing to their unique rigid 3D scaffolds, triptycenes have been extensively explored in a variety of porous polymeric material platforms, such as polymers of intrinsic microporosity (PIMs), conjugated microporous polymers (CMPs), porous aromatic frameworks (PAFs), and covalent triazine frameworks (CTFs).[33−38] A structural inquiry in Cambridge Crystallographic Database on the triptycene-based molecular crystals disclosed that the packings with C−H bonding pointing toward the interlayer space are not unusual (Figures S1 and S2 in the Supporting Information).[39−41] Although the concaved shape of triptycene is supposed to prevent condensed packing, imparting high surface areas, triptycene-derived porous materials are often amorphous and are lacking well-defined pore structures.[42] In contrast, the use of triptycene-based building blocks to prepare highly crystalline COFs/CPs is rare. The successful examples usually require highly symmetric hexafunctionalized monomers and afford 3D COFs with diverse topologies.[43−46] For instance, Fang et al. demonstrated that the use of triptycene-based building blocks could lead to 3D COFs with remarkable gas adsorption capabilities.[43−45] Recently, the triptycene-based linkers were utilized to construct covalently bonded porous organic nanotubes (CONTs), wherein interesting self-assembly properties were observed.[47] There is only one example of crystalline 2D layered COF built with triptycene monomers that benefits from the superior reversibility of the boronate ester linkage. However, the limited persistence of these boronate ester-based materials hampers their potential for long-term utility.[48]

The trifunctional triptycene monomers are synthetically more accessible and compatible with more bridging methods, which makes them appealing building blocks for the construction of dispersible COF materials with weaker interlayer interactions. However, these monomers possess a lower degree of symmetry than hexafunctionalized ones and are usually obtained as a mixture of two regioisomers because of the distinct spatial arrangement of the three functionalities. Probably due to these structural features, the previously reported polymers based on trifunctional triptycene units are all amorphous and access to crystalline 2D COFs/CPs using these trifunctional monomers remains elusive.

On the basis of continuing interests in exploring the unique influence of isomerism on the properties of polymers,[49,50] we envision that the distinct linking group arrangements of

https://doi.org/10.1021/jacsau.2c00214
JACS Au 2022, 2, 1638−1650

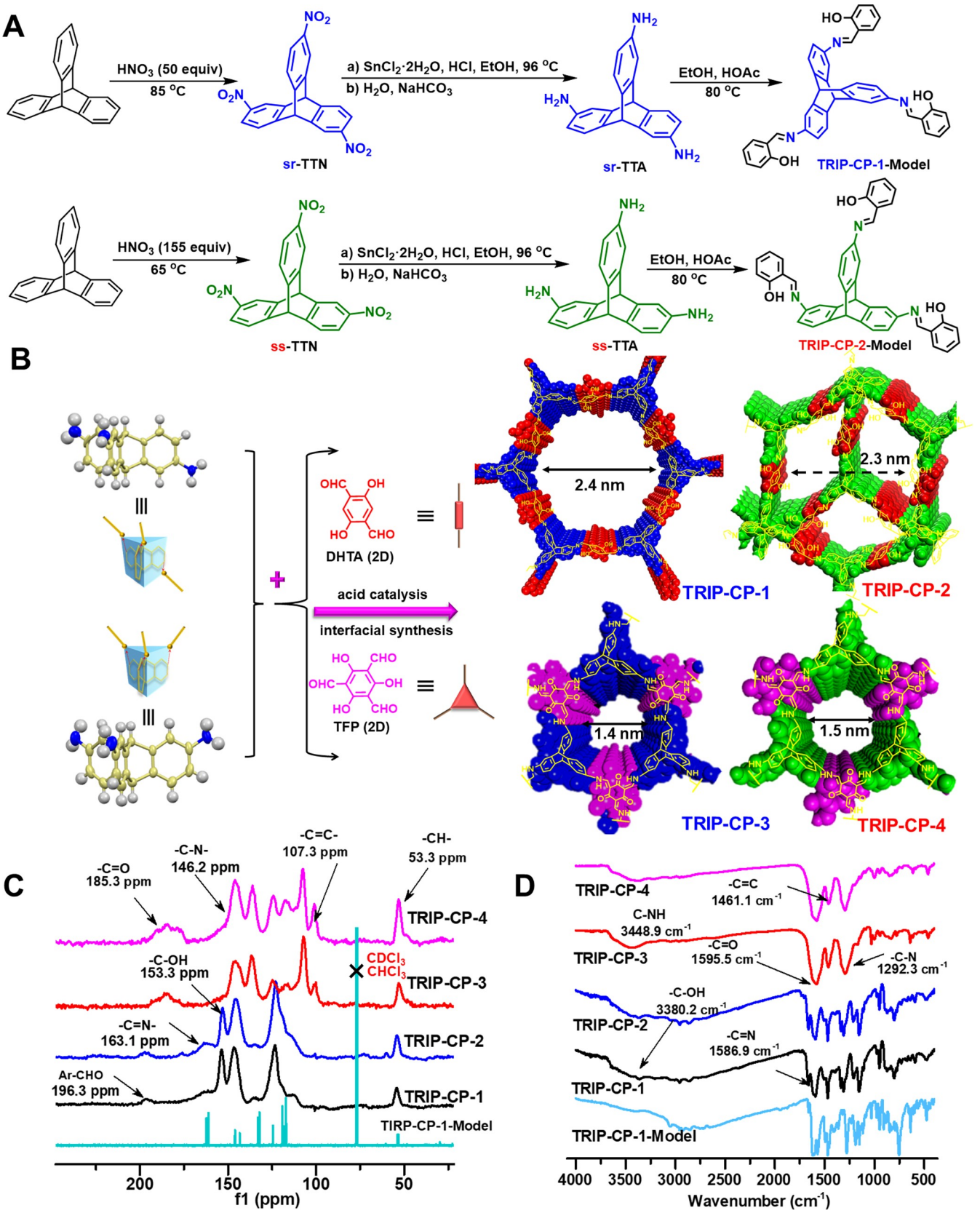

Figure 2. Synthetic route for 3D monomers, simulated structures of the resulting imine-based 2D CPs, and their structural characterizations. (A) Preparation of **sr-TTA**, **ss-TTA**, **TRIP-CP-1-Model**, and **TRIP-CP-2-Model**. (B) Ideal eclipsed AA stacking structures of **TRIP-CP-1** (**sr-TTA +DHTA**), **TRIP-CP-2** (**ss-TTA+DHTA**), **TRIP-CP-3** (**sr-TTA+TFP**), **TRIP-CP-4** (**ss-TTA+TFP**), and their synthetic route. (C) Solid-state ^{13}C cross-polarization/magic-angle sample spinning (CP/MASS) NMR spectra of **TRIP-CPs** and the ^{13}C NMR of **TRIP-CP-1-Model** in $CDCl_3$. (D) Fourier transform infrared (FT-IR) spectra of **TRIP-CPs** and the model compound.

https://doi.org/10.1021/jacsau.2c00214
JACS Au 2022, 2, 1638−1650

trifunctionalized 3D monomers would have a profound influence on the orientation of polymer growth, which in turn allows the manipulation of the crystallinity and the morphology of COFs/CPs via regioisomerism. Herein, we report our efforts to synthesize a series of crystalline and highly dispersive 2D CPs with 3D trifunctional triptycene monomers (Figure 1). Compared with 2D COFs built solely with planar monomers, these COF/CP materials with C−H bonds facing the (100) facets have better dispersibility in solution. Interestingly, the triptycene monomers with functional groups distributed over both sides (lower symmetry) afforded CPs with higher crystallinity than those obtained with C_{3v} symmetrical monomers. Furthermore, the higher crystallinity is accompanied by a higher dispersibility. These findings indicate that the combination of rationally designed 3D monomers and the regioisomerism-based morphology control provides a powerful solution to access highly crystalline few-layer CP nanosheets of excellent dispersibility.

RESULTS AND DISCUSSION

We set out our investigation by synthesizing the amino-containing trifunctional triptycene monomer with the aim to construct dispersible layered COFs/CPs through the well-documented imine-based dynamic chemistry. By design, three nitro groups can be installed through the treatment of triptycene with nitric acid, and a subsequent reduction would afford the desired triamino triptycenes (Figure 2A). Due to the statistical nature of the nitration, a mixture of trinitrotriptycenes with nitro groups positioned differently was envisioned. Effective separation of these two isomers (Figure 2A, **sr-TTN**, and **ss-TTN**) through column chromatography enabled access to a pair of pure triaminotriptycene isomers (Figure 2A, **sr-TTA**, and **ss-TTA**), which allowed us to examine the influence of distinct functional group arrangements on the preparation of CPs. It is noteworthy that monomer **ss-TTA** with all amino groups residing on the same side is C_{3v} symmetrical, whereas its regioisomer **sr-TTA** does not possess any symmetrical plane or axis because the amino groups are distributed on both faces of the triptycene (Figure 2A,B). The chemical structures and the amino group arrangements of these building blocks were unambiguously confirmed by ^{1}H and ^{13}C NMR spectroscopy (Figures S3−S22 in the Supporting Information). We next attempted the condensation between **sr-TTA**/**ss-TTA** and a series of dicarbonyl monomers, such as terephthalaldehyde, and biphenyl dialdehyde with the aim to prepare crystalline dispersive CPs. However, similar to what was observed by others previously,[42] only amorphous cross-linked polymeric materials were obtained even after the extensive screening of reaction solvents and temperatures. This observation may be attributed to the attenuated interlayer interactions, which are not sufficiently strong to direct the formation of stable layered assemblies for the reactions in dilute solution.

Recently, interfacial reactions have attracted increasing attention for the preparation of highly crystalline 2D COF materials, which benefit from the proper reaction kinetics and the high tendency to form nanosheets at the interface. For instance, Banerjee et al. successfully synthesized crystalline 2D COF films that can be used to selectively separate small molecules under interfacial conditions using *p*-toluenesulfonic acid (PTSA) as a catalyst.[19] Dichtel et al. disclosed that the use of a proper Lewis acid is crucial to rapidly access crystalline 2D COF thin films in ambient conditions.[20,21] The effectiveness of the interfacial reaction conditions was also demonstrated in the preparation of nanofiltration membranes and graphene-like nanoribbons.[22−27] Inspired by these successful outcomes, we envisioned that the combination of interfacial reaction conditions and a suitable acid catalyst may allow access to our designed CP materials. Initial attempts using terephthalaldehyde and biphenyl dialdehyde as the monomers did not afford noticeable precipitation or films under interfacial conditions. To make the condensation energetically more favorable, salicylaldehyde-based monomers were used owing to the higher stability of their imine derivatives. In particular, the condensation of 2,5-dihydroxyterephthalaldehyde (**DHTA**) or 2,4,6-triformylphloroglucinol (**TFP**) with the regioisomers **sr-TTA** and **ss-TTA** via [3+2] and [3+3] modes produces four 2D crystalline polymers. As not all these polymers fulfill the criteria generally expected by COFs, such as very high crystallinity and surface area, these four polymers are labeled as **TRIP-CP-1**, **TRIP-CP-2**, **TRIP-CP-3**, and **TRIP-CP-4** (Figure 2B). All these **TRIP-CPs** are obtained under interfacial conditions and the calculated pore sizes for these 2D CPs using the Bragg equation span from 1.4 to 2.4 nm, indicating the versatility of this 2D CP platform to systematically tune the dimension of the pore using distinct building blocks (Figure 2B).

Structural Characterization

We next performed the structural characterization of the four novel **TRIP-CPs** with C−H bonds pointing to the (100) facet using CP−MAS ^{13}C NMR. As depicted in Figure 2C, the signals at 53.3 ppm were attributed to the bridge carbon (−CH−) of the triptycene, which was not observed in CPs constructed solely with 2D planar monomers (Figures S22−S25 in SI). The ^{13}C signals at ca. 163.1 ppm were observed for two imine-linked CPs (**TRIP-CP-1** and **TRIP-CP-2**) using salicylaldehyde monomers, which stemmed from the imine (−C═N−) bonded carbon. As the CPs constructed with **TFP** monomer (**TRIP-CP-3** and **TRIP-CP-4**) had a high tendency to undergo the keto−enol tautomerism, two broad signals at 107.3 and 185.3 ppm were observed, which could be assigned to the exocyclic carbon−carbon double bonds (−C═C−) and the carbonyl carbon (−C═O) motifs, respectively (Figure S28 in SI). It is noteworthy that the ^{13}C resonance related to the terminal amines (−C−NH_2) was not observed, suggesting the high efficiency of polymerization. Consistent with the structural assignments made with CP−MAS ^{13}C NMR, the characteristic absorptions of the (−C═N−) and terminal hydroxyl (−C−OH) stretching at 1595.5 and 3380.2 cm^{-1}, respectively, appear in the infrared (IR) spectra of imine-based CPs shown in Figure 2D. In addition, the IR signal at 1231.3 cm^{-1} can be assigned to the *para*-substituted benzene ring in **TRIP-CP-1** and **TRIP-CP-2**, while the peaks at 3448.9 and 1595.5 cm^{-1} are assigned to the (−C−NH) and (−C═O) stretching in **TRIP-CP-3** and **TRIP-CP-4**, respectively (keto−enol tautomerism). As evidenced by the spectroscopic assignments, the structures of the synthesized CPs are fully consistent with those proposed in Figure 2.

Crystalline Structures

To gain more insights into the crystalline structures of these **TRIP-CPs**, powder X-ray diffraction (PXRD) and high-resolution transmission electron microscopy (HR-TEM) were employed, which are capable of providing crystalline information of the sample as a whole or at local positions, respectively. The structures of **TRIP-CPs** adopting eclipsed AA stacking and three other staggered stacking models were

https://doi.org/10.1021/jacsau.2c00214
JACS Au 2022, 2, 1638−1650

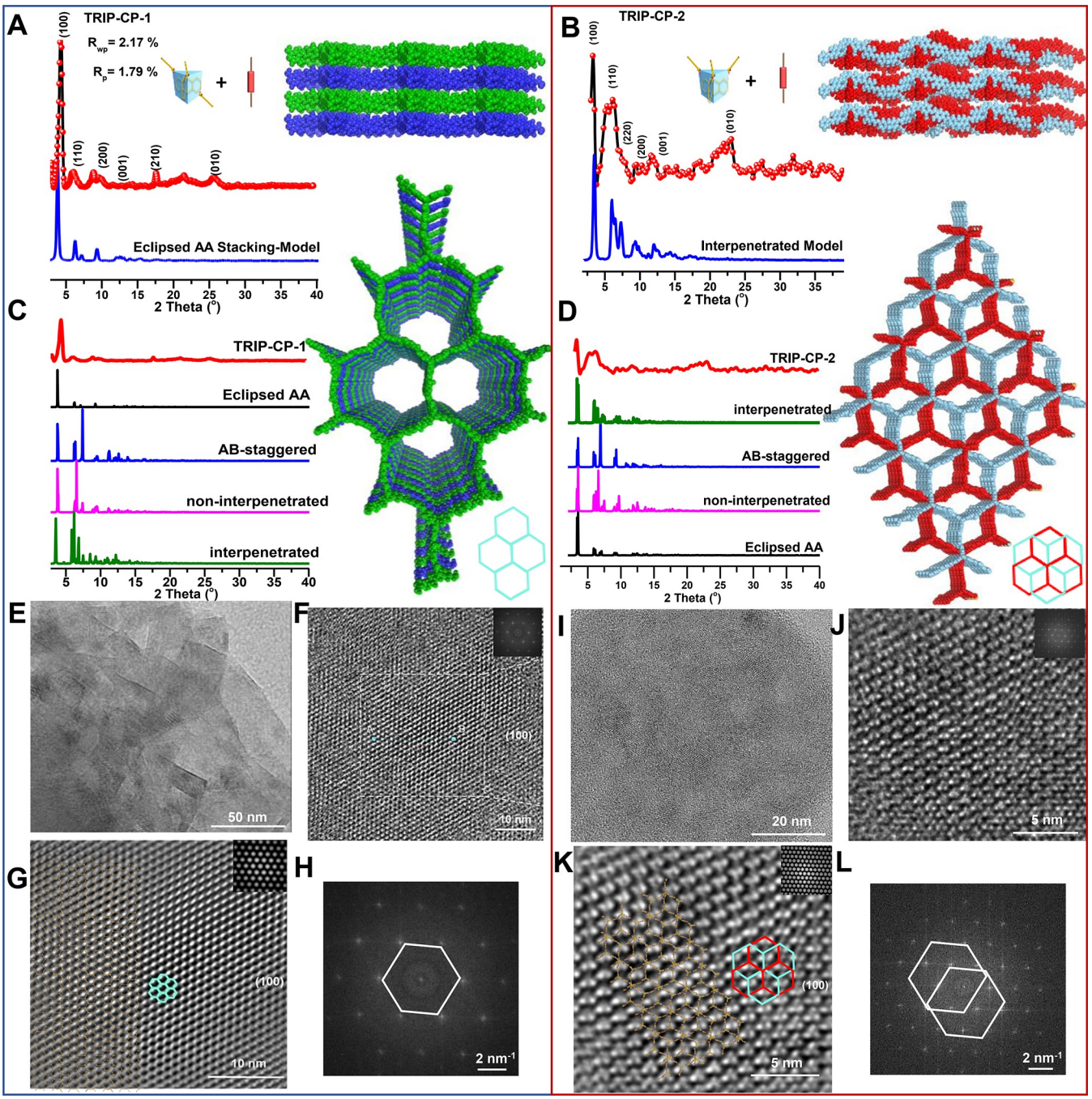

Figure 3. Crystalline structure of **TRIP-CPs**. (A–D) Powder X-ray diffraction (PXRD) patterns of **TRIP-CP-1** and **TRIP-CP-2**. Experimental patterns (red polka dots), refined patterns (black curves), and simulated patterns by Material Studio based on their simulated structures (blue curves). (E–H) HR-TEM images of **TRIP-CP-1** corresponding to the (100) facet (FFT image inset) and the FFT-filtered HR-TEM image corresponding to the (100) facet (inset: masking FFT). (I–L) HR-TEM images of **TRIP-CP-2** corresponding to the (100) facet (FFT image inset) and the FFT-filtered HR-TEM image corresponding to the (100) facet (masking FFT of h inset). R_{wp} denotes the R-weighted pattern.

optimized using Material Studio, and the simulated PXRD patterns were compared with those obtained experimentally (Figures 3 and S29–S41 in SI). As shown in Figure 3A, the strongest PXRD peak for **TRIP-CP-1** is at (3.7° ± 0.1) (8000 counts), which correlates to the diffraction from the (100) facet. Furthermore, the signals at 6.2, 9.3, 12.1, 17.4, and 25.6° are attributed to the diffraction related to the (110), (200), (001), (210), and (010) facets, respectively. The intense signal originating from the (100) plane and the observed multiple diffraction peaks indicate a high level of crystallinity. These CP layers most likely adopt the AA stacking model since the experimentally observed diffractions are in good agreement with the simulated data for the eclipsed AA stacking model (Figures 3A,C and S29–S33 in SI). In contrast to **TRIP-CP-1**, **TRIP-CP-2** built with C_{3v} symmetrical monomers exhibits a chain interpenetrated structure with staggered alignments of CP sheets (Figures 3B,D and S34–S37 in SI). This observation indicates that the spatial arrangement of the functionalities of the 3D monomers is crucial to the formation of highly ordered 2D CP materials. The same behaviors were

https://doi.org/10.1021/jacsau.2c00214
JACS Au 2022, 2, 1638–1650

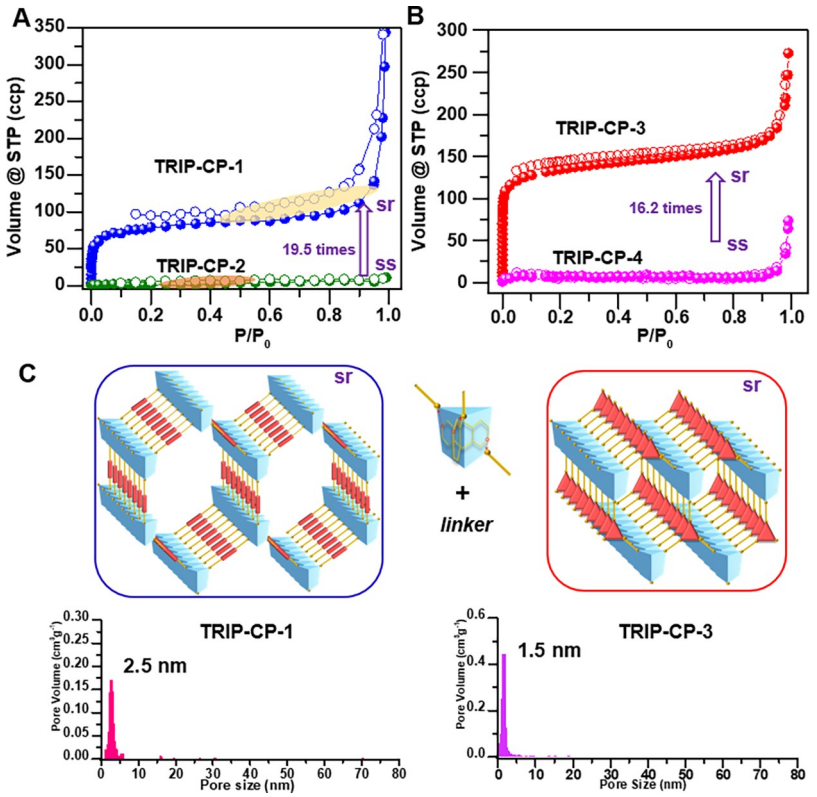

Figure 4. Characterization of the porosity of **TRIP-CPs**. (A, B) Nitrogen adsorption (filled dots) and desorption (unfilled dots) isotherms at 77 K for **TRIP-CP-1**, **TRIP-CP-2**, **TRIP-CP-3**, and **TRIP-CP-4**. (C) Pore size distribution curves are based on nonlocal density functional theory (NLDFT) calculation for **TRIP-CP-1** and **TRIP-CP-3**.

also observed in the preparation of **TRIP-CP-3** (Figure S45 in SI) and **TRIP-CP-4** (Figure S46 in SI), where **TRIP-CP-3** with unsymmetrical monomer **sr-TTA** displayed a higher crystallinity than its isomer **TRIP-CP-4**. As the monomer **ss-TTA** possesses three amino groups on the same face, a cage-like structure is probably formed during the polymerization, making the formation of 2D layered morphology less favorable. In line with this hypothesis, interpenetrations between polymeric chains occurred in **TRIP-CP-2** built with C_{3v} symmetrical monomers (Figure 3D), which may partially explain its lower crystallinity. In contrast, the polymerization of **sr-TTA** is more likely to produce an extended sheet due to the distinct orientation of three amino groups, thereby leading to superior crystallinity. It is noteworthy that the crystallinity of **TRIP-CP-3** is slightly inferior to that of **TRIP-CP-1**, as deduced by the larger linewidth of the XRD peaks. This observation indicates that the reversibility of the condensation between the monomers may also have an influence on the formation of the ordered 2D CPs.

Encouraged by the high crystallinity of **TRIP-CP-1**, we next performed the high-resolution transmission electron microscopy (HR-TEM) analysis to examine its structural integrity, interlayer stacking, and pore size. As depicted in Figures 3 and S52 in SI, the hexagonal channels (Figure 3E−H) and the layered packing of CP sheets were clearly observed in the HR-TEM and the corresponding fast Fourier transform (FFT) images, demonstrating a high level of structural ordering. The measured lattice spacing is larger than 0.5 nm (Figure S53 in SI), which supports the existence of the C−H bond between the layers because the interlayer distance should be smaller than 0.4 nm if $\pi-\pi$ interactions are dominating for assembling the CP layers. The observed pore radius is about 2.5 nm, which is consistent with the value of 2.4 nm calculated based on the PXRD peak at 3.7° ± 0.1. It is noteworthy that the (100) facets of **TRIP-CP-2** were clearly visualized in HR-TEM, providing additional support to the proposed chain interpenetration and staggered alignment of CP sheets (Figures 3I−L and S54 in SI). Furthermore, the HR-TEM image on a larger region revealed that **TRIP-CP-1** synthesized under interfacial conditions tends to form ultrathin nanosheets (Figure S52 in SI). On the other hand, the pore radius observed in HR-TEM for **TRIP-CP-3** is about 1.5 nm (Figure S56 in SI), which is consistent with the pore formed by three **TFP** and three **sr-TTA** units. In contrast to the high crystallinity of **TRIP-CP-1** and **TRIP-CP-3**, no highly ordered region was observed in HR-TEM for **TRIP-CP-4**, which was synthesized with the C_{3v} symmetrical **ss-TTA**. These observations indicate that the use of a low-symmetry 3D monomer with functionalities positioned on distinct faces is crucial for accessing the highly crystalline 2D **TRIP-CPs** with larger interlayer distances.

Porosity Measurements

To further examine the influence of isomeric 3D monomeric units on the pore size and pore size distribution, we performed the Brunauer−Emmett−Teller (BET) surface area measurement of the as-synthesized **TRIP-CPs** (Figure 4A,B). The BET surface areas based on N_2 adsorption for **TRIP-CP-1** and **TRIP-CP-3** were determined to be 371 and 533 $m^2\ g^{-1}$, respectively. In contrast, much lower surface areas were observed for **TRIP-CP-2** (19 $m^2\ g^{-1}$) and **TRIP-CP-4** (33 $m^2\ g^{-1}$). Obviously, the arrangements of the amine groups on the 3D monomer have a pronounced impact not only on crystallinity but also on gas adsorption properties. The

https://doi.org/10.1021/jacsau.2c00214
JACS Au 2022, 2, 1638−1650

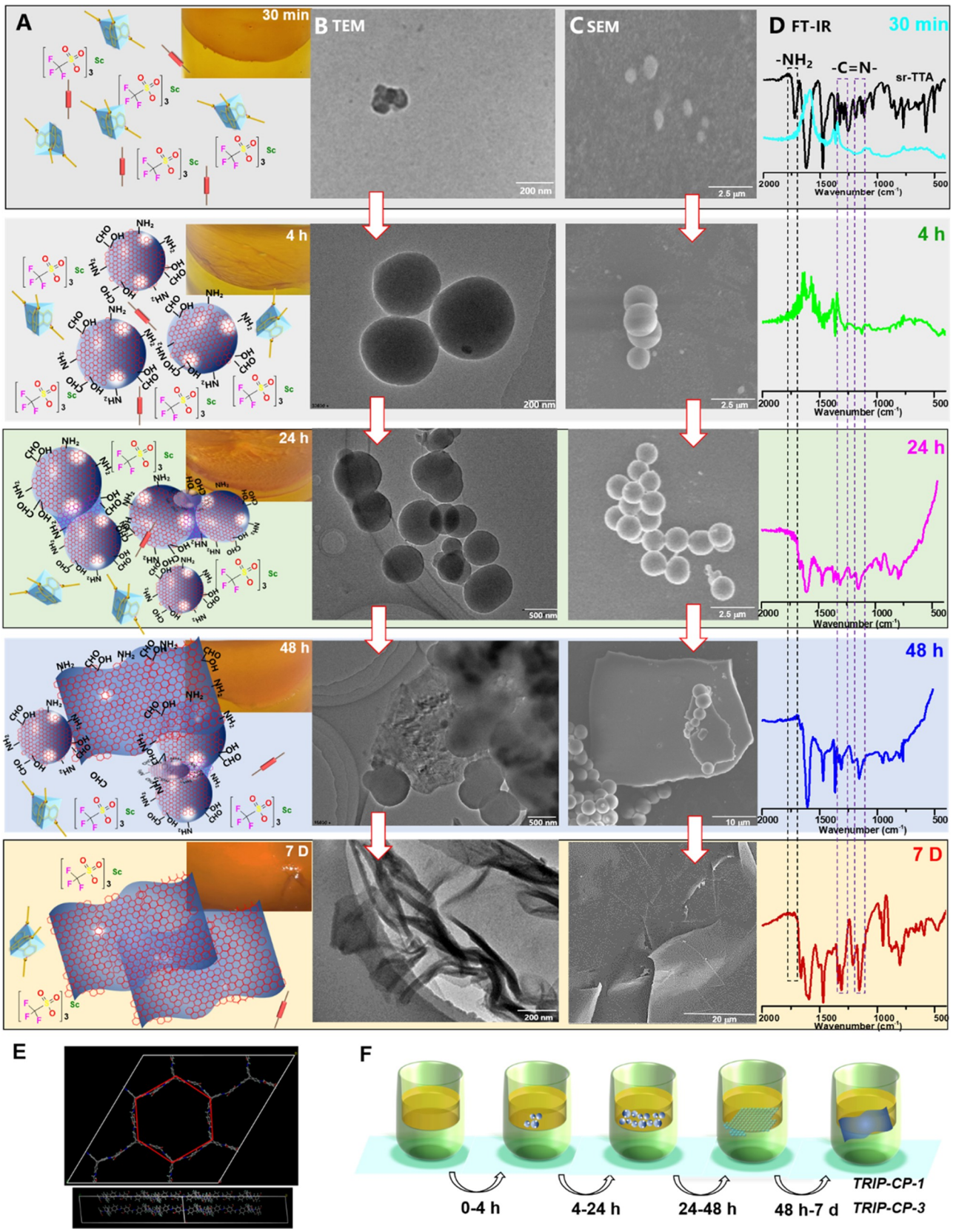

Figure 5. Dynamic morphology evolution of **TRIP-CP-1**. (A) Schematic illustration of the mechanism for the transformation from nanospheres into the film morphology in the presence of $Sc(OTf)_3$. (B–D) Time-dependent TEM and SEM images and FT-IR spectra provide support for the proposed mechanism. (E) Red circle corresponds to a single unit cell of **TRIP-CP-1**. (F) Schematic illustration of time-dependent morphology transformations of **TRIP-CP-1** and **TRIP-CP-3**. Note: In the initial 4 h, the amount of the formed CP is not sufficient for the FT-IR measurements. The observed FT-IR signals are mainly attributed to the KBr pellet.

https://doi.org/10.1021/jacsau.2c00214
JACS Au 2022, 2, 1638–1650

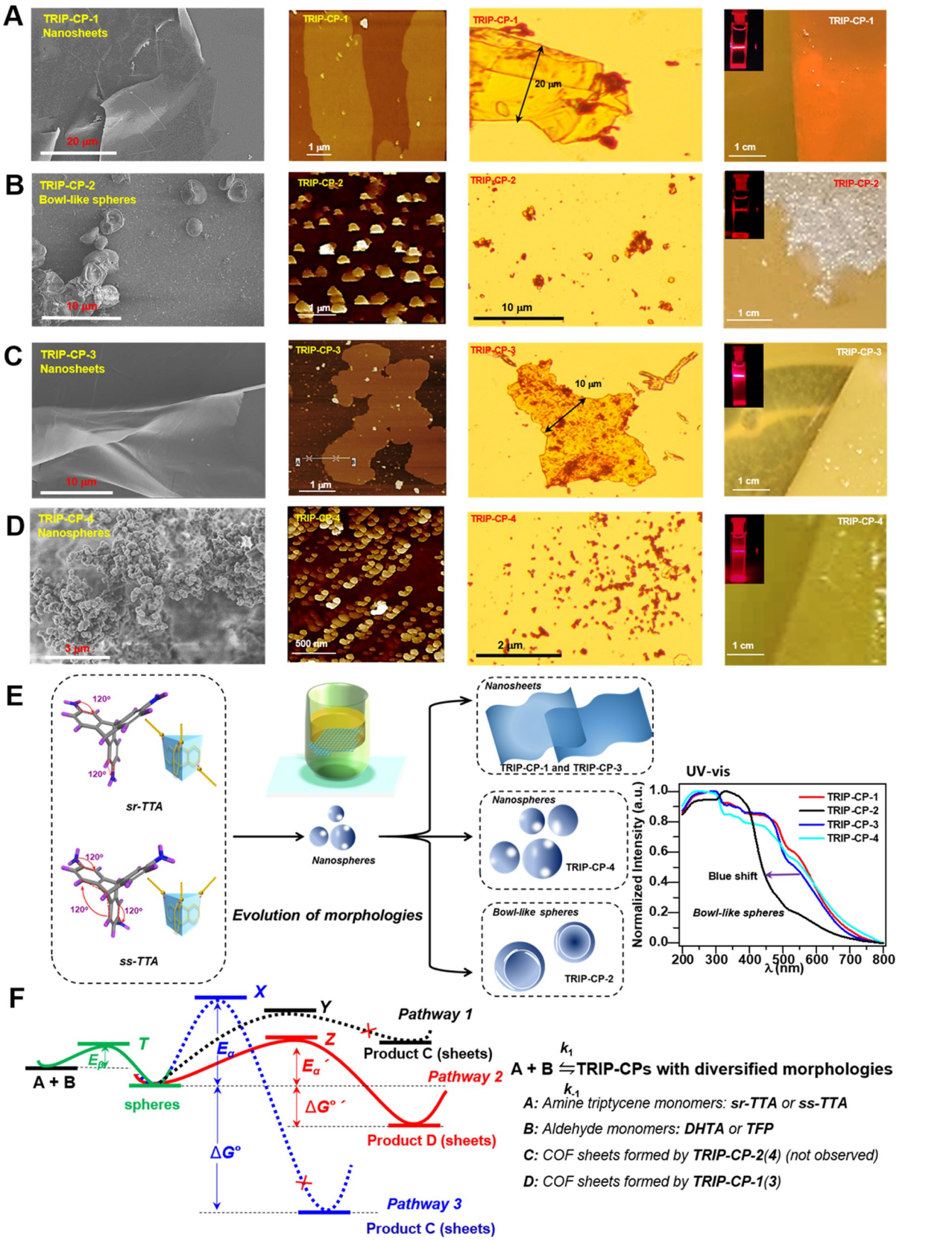

Figure 6. Morphology studies of **TRIP-CPs**. (A–D) SEM images in a large range, AFM images, optical microscopy, and digital camera images on glass slides of **TRIP-CPs** with diverse morphologies (inset: Tyndall effect observed with **TRIP-CPs** dispersion with a concentration of 0.1 mg mL^{-1}). (E) Diversified morphologies of **TRIP-CPs** and their evolution processes charaterized with the Raman and UV–vis spectroscopy. (F) Common energy landscape illustrating the competition between the thermodynamically and kinetically controlled **TRIP-CPs** formation and morphology conversion.

https://doi.org/10.1021/jacsau.2c00214
JACS Au 2022, 2, 1638–1650

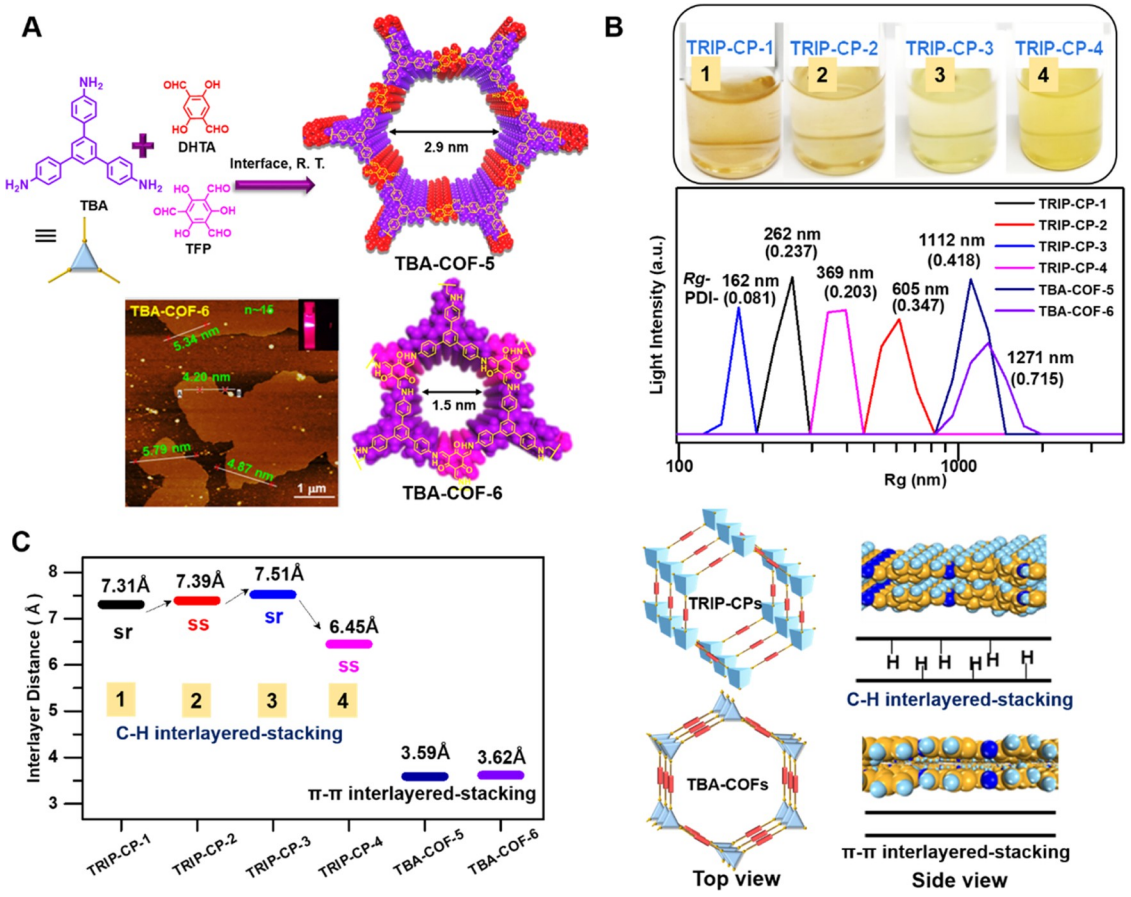

Figure 7. Dispersity and the formation of thin-layer nanosheets. (A) Synthetic route to densely packed **TBA-COF-5** (**TBA+DHTA**) and **TBA-COF-6** (**TBA+TFP**) and AFM image of **TBA-COF-6**. (B) R_g of **TRIP-CP-1**, **TRIP-CP-2**, **TRIP-CP-3**, **TRIP-CP-4**, **TBA-COF-5** (**TBA+DHTA**), and **TBA-COF-6** (**TBA+TFP**) determined by dynamic light scattering (DLS) tests (PDI data by DLS dispersion inset, 0.2 mg mL^{-1}). (C) Calculated interlayered distances.

hysteresis loop, a typical feature of mesoporous material, was observed in the N_2 adsorption/desorption curve for **TRIP-CP-1** shown in Figure 4C, consistent with the simulated pore size. Meanwhile, the calculated pore sizes of 1.4 and 1.5 nm for **TRIP-CP-3** and **TRIP-CP-4** are also in line with the simulated microporous feature. It is noteworthy that the dynamicity of **TRIP-CPs-1** upon triggering by N_2 may also contribute to the observed gap between the adsorption and desorption curve because the inclusion of gas molecules in certain CPs can induce crystal contraction and expansion.[4,5] In our case, the adsorption of N_2 during the surface area measurement may partially dislocate the CP layers, making the desorption process deviating from that occurred in the adsorption. The gap between adsorption and desorption is also observable for **TRIP-CP-2**. However, as **TRIP-CP-2** has a much lower BET surface area compared to that of **TRIP-CP-1** (19 vs 371 m^2 g^{-1}), the magnitude of the gap is smaller. No gap was observed in the N_2 adsorption measurements for **TRIP-CP-3** and **TRIP-CP-4** since they are both microporous materials.

Morphology Studies

The scanning electron microscopy (SEM), atomic force microscopy (AFM), optical microscopy, and transmission electron microscopy (TEM) images and FT-IR spectra were then taken for the as-synthesized **TRIP-CPs** with the aim to investigate the influence of distinct amine group arrangement on morphology. As the reaction proceeded, the morphology for **TRIP-CP-1** was slowly transformed into thin layers (Figure 5), whereas no further evolution of morphology was observed for **TRIP-CP-2** once sphere or hollow sphere structures were formed. As shown in Figure 6A–D, the morphology of **TRIP-CPs** comprising **ss-TTA** and **sr-TTA** differs significantly. Thin-layer morphology was observed for **TRIP-CP-1** and **TRIP-CP-3**, which were composed of low-symmetry **sr-TTA** (Figure 6A,C). In contrast, morphologies of bowl-like spheres and nanospheres (Figure 6B,D) were prevalently observed for **TRIP-CP-2** and **TRIP-CP-4**, supporting a profound impact of functional group arrangements on the morphology. For the monomer **sr-TTA** bearing amino groups at distinct faces, the polycondensation tends to afford an extended planar structure, whereas the polymerization with **ss-TTA** with three amino groups pointing to the same direction would preferentially result in a curved surface, hampering the formation of ordered layered structures (Figure 6E). As a consequence, the distinct morphologies observed may have originated from distinct orientations in CP growth. The UV–vis light absorption was used to evaluate the light absorption ability of **TRIP-CPs** with different morphologies. The optical absorption of **TRIP-CP-2** with bowl-like spheres morphology showed a blue-shift, which could be attributed to the quantum size effect originating from bowl-like sphere morphology as shown in Figure 6E.[51,52] To gain more insights into the impact of regioisomerism on morphology, the formation of **TRIP-CPs** was carefully monitored through the SEM analysis of samples taken at different time periods. It was found that the sphere

https://doi.org/10.1021/jacsau.2c00214
JACS Au 2022, 2, 1638–1650

morphology was preferentially formed for all **TRIP-CPs** initially (Figure S59 in SI). As the reaction proceeded, the morphology of **TRIP-CP-1** and **TRIP-CP-3** was slowly transformed into a thin-layer one (Figure S60 in SI), whereas no further evolution of morphology was observed for **TRIP-CP-2** and **TRIP-CP-4** once sphere or hollow sphere structures were formed. There were two possible reasons for this interesting observation: (1) the sphere morphology was the thermodynamically stable state for these CPs (Figure 6F, pathway (1)) and (2) the activation energy for the morphology conversion was too high and the barrier could not be conquered under the experimental conditions (Figure 6F, pathway (3)). No matter which reason was true, these phenomena illustrated the importance of functional group arrangements and reaction time on the morphology evolution via dynamic covalent chemistry (Figure 6E).[53−55] It was noteworthy that the factors influencing the morphology evolution were very complicated, depending on not only isomerism but also reaction conditions, the ligation methods, the size and topology of the monomers, temperatures, and so on.[19,23] As our studies only explored the influence of regioisomerism on the evolution of morphologies of **TRIP-CPs** prepared under the same conditions. The trend of the morphology evolution we disclosed here was not envisioned to be broadly applicable to other COFs or CPs.

Dispersity and Formation of Thin-Layer Nanosheets

To investigate whether a larger interlayer spacing leads to better dispersibility, we employed dynamic light scattering (DLS) for the analysis of the COF/CPs dispersion in ethanol (Figure 7B). To compare the dispersibility of **TRIP-CPs** built solely with planar monomers, we further synthesized **TBA-COF-5** and **TBA-COF-6** using widely available monomers under interfacial reaction conditions (Figure 7A). Both **TBA-COFs** possess excellent crystallinity (Figures S47−S50 in SI) and BET surface areas (Figure S51 in SI). DLS measurements show that the hydrodynamic radius (R_g) of **TRIP-CPs** is much smaller than 1 μm, whereas the R_g of nanoparticles in the dispersion of **TBA-COF-5** and **TBA-COF-6** spans from 1 to 2 μm. It is noteworthy that the DLS measurements for **TBA-COF-5** and **TBA-COF-6** have to be performed immediately after sonication because they precipitate quickly when the solution is undisturbed. In contrast, the dispersion of **TRIP-CP-1** remains stable for at least 48 h at a concentration of 0.2 mg mL^{-1}. These observations support the fact that **TRIP-CPs** are more facilely dispersed in solution compared to COFs assembled with strong interlayer $\pi-\pi$ stacking interaction. The enhanced dispersibility likely originates from the weaker interlayer interaction, which facilitates the formation of ultrathin nanosheets. To get more insights into the interlayer interactions for **TRIP-CPs** and **TBA-COFs**, the energies for stacking the hexagonal building units were simulated (Figure S61 in SI). It is found that the stacking energies for **TRIP-CP-1** (D_1 = 272.1 kJ mol^{-1}) and **TRIP-CP-3** (D_3 = 113.1 kJ mol^{-1}) are much smaller compared to those for **TBA-COF-5** (D_5 = 616.9 kJ mol^{-1}) and **TBA-COF-6** (D_6 = 383.5 kJ mol^{-1}). These results are in line with the observation that the dispersibilities of **TRIP-CPs** are better than those of 2D COFs with strong $\pi-\pi$ stackings. Notably, the hydrogens of the OH groups of **TRIP-CPs** have already engaged in the intramolecular hydrogen bonding with the imine groups, significantly lowering their capability to serve as a hydrogen-bond donor. Owing to the large distance (7 Å) between the CP layers, the hydroxyl groups residing in different layers are too far to participate in hydrogen bonding. The high dispersibility of **TRIP-CPs** is also consistent with the observations of the atomic force microscopy (AFM) experiments, where the thickness of the nanosheets from **TRIP-CP-1** varies between 3.26 and 3.78 nm (Figure 5A), while **TRIP-CP-3** produces nanosheets with thicknesses varying from 3.0 to 4.0 nm (Figure 7C). These thicknesses correlate to a layer number of about 5. In contrast, the average thickness of **TBA-COF-6** built solely with 2D planar monomers (Figure 7A) nanosheets is in the range of 4.20−5.79 nm, equivalent to the dense packing of about 15 layers of unit cells. These observations indicate that the use of 3D triptycene-based building blocks can induce larger interlayer *d*-spacings and lead to CP materials that are easily exfoliated to few-layer nanosheets. As a consequence, access to CP materials assembled with interactions between C−H bonds using monomers of unique topologies may serve as a new strategy to facilitate the exfoliation of 2D CPs into ultrathin CP nanosheets.

CONCLUSIONS

In summary, we have prepared a series of **TRIP-CPs** using 3D trifunctional triptycene-based monomers. These materials possess layered 2D structures, and the assembly of layers is stabilized by relatively weak van der Waals interactions between C−H bonds pointing to the (100) facet other than the usual $\pi-\pi$ stackings, endowing **TRIP-CPs** with superior dispersibility in solution. It is further found that the arrangement of amino groups on the 3D triptycene monomer has a profound influence on the crystallinity of the produced **TRIP-CPs** under interfacial conditions. The monomer **sr-TTA** of low-symmetry afforded **TRIP-CPs** with higher crystallinity compared to those built with the C_{3v} symmetric **ss-TTA**. The regioisomerism of 3D monomers also plays a crucial role in controlling the morphology of the corresponding CP materials. These findings disclosed that high crystallinity and high dispersity can be simultaneously imparted into 2D layered COFs/CPs via the manipulation of the linking group arrangements of proper 3D monomers. We envision that the strategy and insights we disclosed here will promote the development of more dispersive CPs tailored for diverse applications.

MATERIALS AND METHODS

Fourier transform infrared (FT-IR) spectra were collected in the transmission mode (4000−400 cm^{-1}) using a Nicolet iS10 FT-IR spectrometer (Thermo Fisher Scientific). The ^{1}H NMR spectra were measured on an Agilent AV400 spectrometer (400 MHz). The ^{13}C NMR spectra were measured on a Bruker AV600 spectrometer (600 MHz). The Brunauer−Emmett−Teller (BET) surface areas and pore sizes were measured by the BELSORP MR6 (BEL, Japan) surface area and porosity analyzer. Solid-State ^{13}C CP/MAS NMR spectra were measured by a WB 600 MHz Bruker Germany, Advance II spectrometer. The particle size tests of covalent organic frameworks were tested by a dynamic light scattering particle size distribution analyzer Zetasizer Nano-ZS90 (Malvern, British, test range 0.3−5 μm). Powder X-ray diffraction (XRD) patterns were measured by an X'celerator detector (X'Pert Pro MPD, Panalytical Co.). Transmission electron microscopy (TEM) images were observed by a TEM JEM-2100F (JEOL Japan) microscope. High-resolution field emission scanning electron microscopy (SEM) images of resulting samples were measured by a JSM-6390LV microscope (Japan Electronics Corporation). High-resolution field transmission electron microscopy (HR-TEM) images were also observed by a TEM JEM-2100F (JEOL Japan) microscope. Layered morphologies were observed by atomic

https://doi.org/10.1021/jacsau.2c00214
JACS Au 2022, 2, 1638−1650

force microscopy (scanning probe microscopy SPM-9700 instrument, Shimadzu Japan). For the HR-TEM image tests, the beam damage of the COFs or CPs was usually inevitable and we could observe the damage and disappearance of the crystalline domain during the TEM test in a few seconds. As a consequence, the HR-TEM equipment and probe were also very important and the image should be taken before the sample was damaged. We recommend the use of a TEM JEM-2100F (JEOL Japan) microscope or Talosf200x (FEI Holland). These instruments support fast navigation, which allows rapid and accurate energy-dispersive spectroscopy (EDS) analysis in all dimensions, one-dimensional to four-dimensional (1D−4D), and often produces good HR-TEM images. On the other hand, the TEM beam should not be focused on the COF sample for too long to avoid beam damage. As a result, a series of operations of adjusting the focal length and the gray scale must be completed in a short time to capture the area of interest.

■ ASSOCIATED CONTENT

Supporting Information

The Supporting Information is available free of charge at https://pubs.acs.org/doi/10.1021/jacsau.2c00214.

Instruments; synthetic procedures; HR-MS; NMR; FT-IR, solid-state ^{13}C NMR; PXRD; SEM; TEM; HR-TEM; UV−vis spectra; nitrogen sorption curves; and DLS measurements (PDF)

■ AUTHOR INFORMATION

Corresponding Authors

Shangbin Jin − *School of Chemical Engineering and Technology, Xi'an Jiaotong University, Xi'an, Shaanxi 710049, China;* orcid.org/0000-0002-2456-3540; Email: shangbin@xjtu.edu.cn

Yanchuan Zhao − *Key Laboratory of Organofluorine Chemistry, Shanghai Institute of Organic Chemistry, University of Chinese Academy of Sciences, Chinese Academy of Sciences, Shanghai 200032, China; Key Laboratory of Energy Regulation Materials, Shanghai Institute of Organic Chemistry, Chinese Academy of Sciences, Shanghai 200032, China;* orcid.org/0000-0002-2903-4218; Email: zhaoyanchuan@sioc.ac.cn

Authors

Siquan Zhang − *Key Laboratory of Organofluorine Chemistry, Shanghai Institute of Organic Chemistry, University of Chinese Academy of Sciences, Chinese Academy of Sciences, Shanghai 200032, China;* orcid.org/0000-0001-7057-7778

Nie Fang − *Key Laboratory of Organofluorine Chemistry, Shanghai Institute of Organic Chemistry, University of Chinese Academy of Sciences, Chinese Academy of Sciences, Shanghai 200032, China*

Xiaonan Ji − *Key Laboratory of Organofluorine Chemistry, Shanghai Institute of Organic Chemistry, University of Chinese Academy of Sciences, Chinese Academy of Sciences, Shanghai 200032, China*

Yuefei Gu − *Key Laboratory of Organofluorine Chemistry, Shanghai Institute of Organic Chemistry, University of Chinese Academy of Sciences, Chinese Academy of Sciences, Shanghai 200032, China*

Zhenchuang Xu − *Key Laboratory of Organofluorine Chemistry, Shanghai Institute of Organic Chemistry, University of Chinese Academy of Sciences, Chinese Academy of Sciences, Shanghai 200032, China*

Complete contact information is available at: https://pubs.acs.org/10.1021/jacsau.2c00214

Notes

The authors declare no competing financial interest.

■ ACKNOWLEDGMENTS

This work was supported by the Strategic Priority Research Program of the Chinese Academy of Sciences (XDC06020102) and the National Natural Science Foundation of China (Nos. 2187129 and 91956120). S.Q. thanks Wenjie Zhu, Qi Jia, and Yixuan Chen for their help with NMR and DLS measurements.

■ REFERENCES

(1) Côté, A. P.; Benin, A. I.; Ockwig, N. W.; O'Keeffe, M.; Matzger, A. J.; Yaghi, O. M. Porous, Crystalline, Covalent Organic Frameworks. *Science* **2005**, *310*, 1166−1170.

(2) Ding, S.-Y.; Gao, J.; Wang, Q.; Zhang, Y.; Song, W.-G.; Su, C.-Y.; Wang, W. Construction of Covalent Organic Framework for Catalysis: Pd/COF-LZU1 in Suzuki-Miyaura Coupling Reaction. *J. Am. Chem. Soc.* **2011**, *133*, 19816−19822.

(3) Dalapati, S.; Jin, E.; Addicoat, M.; Heine, T.; Jiang, D. Highly Emissive Covalent Organic Frameworks. *J. Am. Chem. Soc.* **2016**, *138*, 5797−5800.

(4) Ding, S.-Y.; Wang, W. Covalent organic frameworks (COFs). From design to applications. *Chem. Soc. Rev.* **2013**, *42*, 548−568.

(5) Rodríguez-San-Miguel, D.; Zamora, F. Processing of covalent organic frameworks: an ingredient for a material to succeed. *Chem. Soc. Rev.* **2019**, *48*, 4375−4386.

(6) Shao, P.; Li, J.; Chen, F.; Ma, L.; Li, Q.; Zhang, M.; Zhou, J.; Yin, A.; Feng, X.; Wang, B. Flexible Films of Covalent Organic Frameworks with Ultralow Dielectric Constants under High Humidity. *Angew. Chem., Int. Ed.* **2018**, *57*, 16501−16505.

(7) Hao, Q.; Zhao, C.; Sun, B.; Lu, C.; Liu, J.; Liu, M.; Wan, L. J.; Wang, D. Confined Synthesis of Two-Dimensional Covalent Organic Framework Thin Films within Superspreading Water Layer. *J. Am. Chem. Soc.* **2018**, *140*, 12152−12158.

(8) Huang, N.; Chen, X.; Krishna, R.; Jiang, D. Two-Dimensional Covalent Organic Frameworks for Carbon Dioxide Capture through Channel-Wall Functionalization. *Angew. Chem., Int. Ed.* **2015**, *54*, 2986−2990.

(9) Medina, D. D.; Rotter, J. M.; Hu, Y.; Dogru, M.; Werner, V.; Auras, F.; Markiewicz, J. T.; Knochel, P.; Bein, T. Room temperature synthesis of covalent-organic framework films through vapor-assisted conversion. *J. Am. Chem. Soc.* **2015**, *137*, 1016−1019.

(10) Smith, B. J.; Overholts, A. C.; Hwang, N.; Dichtel, W. R. Insight into the crystallization of amorphous imine-linked polymer networks to 2D covalent organic frameworks. *Chem. Commun.* **2016**, *52*, 3690−3693.

(11) Evans, A. M.; Parent, L. R.; Flanders, N. C.; Bisbey, R. P.; Vitaku, E.; Kirschner, M. S.; Schaller, R. D.; Chen, L. X.; Gianneschi, N. C.; Dichtel, W. R. Seeded growth of single-crystal two-dimensional covalent organic frameworks. *Science* **2018**, *361*, 52−57.

(12) Ma, T.; Kapustin, E. A.; Yin, S. X.; Liang, L.; Zhou, Z.; Niu, J.; Li, L.-H.; Wang, Y.; Su, J.; Li, J.; Wang, X.; Wang, W. D.; Wang, W.; Sun, J.; Yaghi, O. M. Single-crystal x-ray diffraction structures of covalent organic frameworks. *Science* **2018**, *361*, 48−52.

(13) Han, X.; Zhang, J.; Huang, J.; Wu, X.; Yuan, D.; Liu, Y.; Cui, Y. Chiral induction in covalent organic frameworks. *Nat. Commun.* **2018**, *9*, No. 1294.

(14) Liang, R. R.; Jiang, S. Y.; A, R. H.; Zhao, X. Two-dimensional covalent organic frameworks with hierarchical porosity. *Chem. Soc. Rev.* **2020**, *49*, 3920−3951.

(15) Zhou, T. Y.; Xu, S. Q.; Wen, Q.; Pang, Z. F.; Zhao, X. One-step construction of two different kind s of pores in a 2D covalent organic framework. *J. Am. Chem. Soc.* **2014**, *136*, 15885−15888.

(16) Guo, X.; Lin, E.; Gao, J.; Mao, T.; Yan, D.; Cheng, P.; Ma, S.; Chen, Y.; Zhang, Z. Rational Construction of Borromean Linked Crystalline Organic Polymers. *Angew. Chem., Int. Ed.* **2021**, *60*, 2974−2979.
(17) Garai, B.; Shetty, D.; Skorjanc, T.; et al. Taming the Topology of Calix[4]arene-Based 2D-Covalent Organic Frameworks: Interpenetrated vs Noninterpenetrated Frameworks and Their Selective Removal of Cationic Dyes. *J. Am. Chem. Soc.* **2021**, *143*, 3407−3415.
(18) Zhu, Q.; Wang, X.; Clowes, R.; Cui, P.; Chen, L.; Little, M. A.; Cooper, A. I. 3D Cage COFs: A Dynamic Three-Dimensional Covalent Organic Framework with High-Connectivity Organic Cage Nodes. *J. Am. Chem. Soc.* **2020**, *142*, 16842−16848.
(19) Dey, K.; Pal, M.; Rout, K. C.; H, S. K.; Das, A.; Mukherjee, R.; Kharul, U. K.; Banerjee, R. Selective Molecular Separation by Interfacially Crystallized Covalent Organic Framework Thin Films. *J. Am. Chem. Soc.* **2017**, *139*, 13083−13091.
(20) Matsumoto, M.; Dasari, R. R.; Ji, W.; Feriante, C. H.; Parker, T. C.; Marder, S. R.; Dichtel, W. R. Rapid, Low Temperature Formation of Imine-Linked Covalent Organic Frameworks Catalyzed by Metal Triflates. *J. Am. Chem. Soc.* **2017**, *139*, 4999−5002.
(21) Matsumoto, M.; Valentino, L.; Stiehl, G. M.; Balch, H. B.; Corcos, A. R.; Wang, F.; Ralph, D. C.; Mariñas, B. J.; Dichtel, W. R. Lewis-Acid-Catalyzed Interfacial Polymerization of Covalent Organic Framework Films. *Chem* **2018**, *4*, 308−317.
(22) Guo, Y.; Nuermaimaiti, A.; Kjeldsen, N. D.; Gothelf, K. V.; Linderoth, T. R. Two-Dimensional Coordination Networks from Cyclic Dipeptides. *J. Am. Chem. Soc* **2020**, *142*, 19814−19818.
(23) Sasmal, H. S.; Halder, A.; Kunjattu, H. S.; Dey, K.; Nadol, A.; Ajithkumar, T. G.; Ravindra Bedadur, P.; Banerjee, R. Covalent Self-Assembly in Two Dimensions: Connecting Covalent Organic Framework Nanospheres into Crystalline and Porous Thin Films. *J. Am. Chem. Soc.* **2019**, *141*, 20371−20379.
(24) Shi, X.; Ma, D.; Xu, F.; Zhang, Z.; Wang, Y. Table-salt enabled interface-confined synthesis of covalent organic framework (COF) nanosheets. *Chem. Sci.* **2020**, *11*, 989−996.
(25) Li, Y.; Guo, L.; Lv, Y.; Zhao, Z.; Ma, Y.; Chen, W.; Xing, G.; Jiang, D.; Chen, L. Polymorphism of 2D Imine Covalent Organic Frameworks. *Angew. Chem., Int. Ed.* **2021**, *60*, 5363−5369.
(26) Veber, G.; Diercks, C. S.; Rogers, C.; Perkins, W. S.; Ciston, J.; Lee, K.; Llinas, J. P.; Liebman-Peláez, A.; Zhu, C.; Bokor, J.; Fischer, F. R. Reticular Growth of Graphene Nanoribbon 2D Covalent Organic Frameworks. *Chem* **2020**, *6*, 1125−1133.
(27) Cao, L.; Wu, H.; Cao, Y.; Fan, C.; Zhao, R.; He, X.; Yang, P.; Shi, B.; You, X.; Jiang, Z. Weakly Humidity-Dependent Proton-Conducting COF Membranes. *Adv. Mater.* **2020**, *32*, No. 2005565.
(28) Chen, X.; Li, Y.; Wang, L.; Xu, Y.; Nie, A.; Li, Q.; Wu, F.; Sun, W.; Zhang, X.; Vajtai, R.; Ajayan, P. M.; Chen, L.; Wang, Y. High-Lithium-Affinity Chemically Exfoliated 2D Covalent Organic Frameworks. *Adv. Mater.* **2019**, *31*, No. 1901640.
(29) Wang, X.; Fu, Z.; Zheng, L.; Zhao, C.; Wang, X.; Chong, S. Y.; McBride, F.; Raval, R.; Bilton, M.; Liu, L.; Wu, X.; Chen, L.; Sprick, R. S.; Cooper, A. I. Covalent Organic Framework Nanosheets Embedding Single Cobalt Sites for Photocatalytic Reduction of Carbon Dioxide. *Chem. Mater.* **2020**, *32*, 9107−9114.
(30) Li, X.; Xu, H. S.; Leng, K.; Chee, S. W.; Zhao, X.; Jain, N.; Xu, H.; Qiao, J.; Gao, Q.; Park, I. H.; Quek, S. Y.; Mirsaidov, U.; Loh, K. P. Partitioning the interlayer space of covalent organic frameworks by embedding pseudorotaxanes in their backbones. *Nat. Chem.* **2020**, *12*, 1115−1122.
(31) Zhou, T. Y.; Lin, F.; Li, Z. T.; Zhao, X. Single-step solution-phase synthesis of free-standing two-dimensional polymers and their evolution into hollow spheres. *Macromolecules* **2013**, *46*, 7745−7752.
(32) Rodríguez-San-Miguel, D.; Montoro, C.; Zamora, F. Covalent organic framework nanosheets: preparation, properties, and applications. *Chem. Soc. Rev.* **2020**, *49*, 2291−2302.
(33) Sydlik, S. A.; Chen, Z.; Swager, T. M. Triptycene Polyimides: Soluble Polymers with High Thermal Stability and Low Refractive Indices. *Macromolecules* **2011**, *44*, 976−980.
(34) Chen, J.-J.; Zhai, T.-L.; Chen, Y.-F.; Geng, S.; Yu, C.; Liu, J.-M.; Wang, L.; Tan, B.; Zhang, C. A triptycene-based two-dimensional porous organic polymeric nanosheet. *Polym. Chem.* **2017**, *8*, 5533−5538.
(35) Ikai, T.; Yoshida, T.; Awata, S.; Wada, Y.; Maeda, K.; Mizuno, M.; Swager, T. M. Circularly Polarized Luminescent Triptycene-Based Polymers. *ACS Macro Lett.* **2018**, *7*, 364−369.
(36) Li, P.; Li, P.; Ryder, M. R.; Liu, Z.; Stern, C. L.; Farha, O. K.; Stoddart, J. F. Interpenetration Isomerism in Triptycene-Based Hydrogen-Bonded Organic Frameworks. *Angew. Chem., Int. Ed.* **2019**, *58*, 1664−1669.
(37) Zhao, Y.; He, Y.; Swager, T. M. Porous Organic Polymers via Ring Opening Metathesis Polymerization. *ACS Macro Lett.* **2018**, *7*, 300−304.
(38) Shi, Y.; Hu, K.; Cui, Y.; Cheng, J.; Zhao, W.; Li, X. Magnetic triptycene-based covalent triazine frameworks for the efficient extraction of anthraquinones in slimming tea followed by UHPLC-FLD detection. *Microchem. J.* **2019**, *146*, 525−533.
(39) Lou, K.; Prior, A. M.; Wiredu, B.; Desper, J.; Hua, D. H. Synthesis of Cyclododeciptycene Quinones. *J. Am. Chem. Soc.* **2010**, *132*, 17635−17641.
(40) Tian, X.-H.; Chen, C.-F. Triptycene-Derived Calix[6]arenes: Synthesis, Structures, and Their Complexation with Fullerenes C60 and C70. *Chem. - Eur. J.* **2010**, *16*, 8072−8079.
(41) Tian, X.-H.; Hao, X.; Liang, T.-L.; Chen, C.-F. Triptycene-derived calix[6]arenes: synthesis, structure and tubular assemblies in the solid state. *Chem. Commun.* **2009**, 6771−6773.
(42) Preet, K.; Gupta, G.; Kotal, M.; Kansal, S. K.; Salunke, D. B.; Sharma, H. K.; Sahoo, S. C.; Van Der Voort, P.; Roy, S. Mechanochemical Synthesis of a New Triptycene-Based Imine-Linked Covalent Organic Polymer for Degradation of Organic Dye. *Cryst. Growth Des.* **2019**, *19*, 2525−2530.
(43) Li, H.; Ding, J.; Guan, X.; Chen, F.; Li, C.; Zhu, L.; Xue, M.; Yuan, D.; Valtchev, V.; Yan, Y.; Qiu, S.; Fang, Q. Three-Dimensional Large-Pore Covalent Organic Framework with stp Topology. *J. Am. Chem. Soc.* **2020**, *142*, 13334−13338.
(44) Li, H.; Chen, F.; Guan, X.; Li, J.; Li, C.; Tang, B.; Valtchev, V.; Yan, Y.; Qiu, S.; Fang, Q. Three-Dimensional Triptycene-Based Covalent Organic Frameworks with ceq or acs Topology. *J. Am. Chem. Soc.* **2021**, *143*, 2654−2659.
(45) Yu, C.; Li, H.; Wang, Y.; Suo, J.; Guan, X.; Wang, R.; Valtchev, V.; Yan, Y.; Qiu, S.; Fang, Q. Three-Dimensional Triptycene-Functionalized Covalent Organic Frameworks with hea Net for Hydrogen Adsorption. *Angew. Chem.* **2022**, *134*, No. e202117101.
(46) Li, Z.; Sheng, L.; Wang, H.; Wang, X.; Li, M.; Xu, Y.; Cui, H.; Zhang, H.; Liang, H.; Xu, H.; He, X. Three-Dimensional Covalent Organic Framework with ceq Topology. *J. Am. Chem. Soc.* **2021**, *143*, 92−96.
(47) Koner, K.; Karak, S.; Kandambeth, S.; Karak, S.; Thomas, N.; Leanza, L.; Perego, C.; Pesce, L.; Capelli, R.; Moun, M.; Bhakar, M.; Ajithkumar, T. G.; Pavan, G. M.; Banerjee, R. Porous covalent organic nanotubes and their assembly in loops and toroids. *Nat. Chem.* **2022**, *14*, 507−514.
(48) Kahveci, Z.; Islamoglu, T.; Shar, G. A.; Ding, R.; El-Kaderi, H. M. Targeted synthesis of a mesoporous triptycene-derived covalent organic framework. *CrystEngComm* **2013**, *15*, 1524−1527.
(49) Chen, S.; Zhao, Y. Poly(o-xylylene)s via Cobalt-Catalyzed Reductive Polymerization. *Chin. J. Chem.* **2020**, *38*, 952−958.
(50) Lv, J.; Chen, S.; Xu, Z.; Zhang, S.; Li, Y.; Zhao, Y. Synthesis and Characterization of Diastereoisomeric Polyesters Derived from Bisphenols Bearing Vicinal Trifluoromethyl Groups. *Macromolecules* **2021**, *54*, 3716−3724.
(51) Hu, X.; Zhan, Z.; Zhang, J.; Hussain, I.; Tan, B. Immobilized covalent triazine frameworks films as effective photocatalysts for hydrogen evolution reaction. *Nat. Commun.* **2021**, *12*, No. 6596.
(52) Wang, N.; Cheng, G.; Guo, L.; Tan, B.; Jin, S. Hollow Covalent Triazine Frameworks with Variable Shell Thickness and Morphology. *Adv. Fun. Mater.* **2019**, *29*, No. 1904781.

https://doi.org/10.1021/jacsau.2c00214
JACS Au 2022, 2, 1638−1650

(53) Ji, Q.; Lirag, R. C.; Miljanić, O. Š. Kinetically controlled phenomena in dynamic combinatorial libraries. *Chem. Soc. Rev.* **2014**, *43*, 1873−1884.
(54) Sevim, S.; Sorrenti, A.; Franco, C.; Furukawa, S.; Pané, S.; deMello, A. J.; Puigmartí-Luis, J. Self-assembled materials, and supramolecular chemistry within microfluidic environments: from common thermodynamic states to non-equilibrium structures. *Chem. Soc. Rev.* **2018**, *47*, 3788−3803.
(55) Wang, Y.; He, J.; Liu, C.; Chong, W. H.; Chen, H. Thermodynamics versus kinetics in nanosynthesis. *Angew. Chem., Int. Ed.* **2015**, *54*, 2022−2051.

https://doi.org/10.1021/jacsau.2c00214
JACS Au 2022, 2, 1638−1650